Aerodynamic Shape Optimization for Delaying Dynamic Stall of Airfoils Using Cokriging Regression

Vishal Raul*, and Leifur Leifsson†
Iowa State University, Ames, Iowa, 50011, USA

The dynamic stall phenomenon produces adverse aerodynamic loading, which negatively affects the structural strength and life of aerodynamic systems. Aerodynamic shape optimization (ASO) provides a practical approach for delaying and mitigating dynamic stall characteristics without the addition of an auxiliary system. A typical ASO investigation requires multiple evaluations of accurate but time-consuming computational fluid dynamics (CFD) simulations. In the case of dynamic stall, unsteady CFD simulations are required for airfoil shape evaluation; combining it with high-dimensions of airfoil shape parameterization renders the ASO investigation computationally costly. In this study, metamodel-based optimization (MBO) is proposed using the multifidelity modeling (MFM) technique to efficiently conduct ASO investigation for computationally expensive dynamic stall cases. MFM methods combine data from accurate high-fidelity (HF) simulations and fast low-fidelity (LF) simulations to provide accurate and fast predictions. In particular, Cokriging regression is used for approximating the objective and constraint functions. The airfoil shape is parameterized using six PARSEC parameters. The objective and constraint functions are evaluated for a sinusoidally oscillating airfoil with the unsteady Reynolds-averaged Navier-Stokes equations at a Reynolds number of 135,000, Mach number of 0.1, and reduced frequency of 0.05. The initial metamodel is generated using 220 LF and 20 HF samples. The metamodel is then sequentially refined using the expected improvement infill criteria and validated with the normalized root mean square error. The refined metamodel is utilized for finding the optimal design. The optimal airfoil shape shows higher thickness, larger leading-edge radius, and an aft camber compared to baseline (NACA 0012). The optimal shape delays the dynamic stall occurrence by 3° and reduces the peak aerodynamic coefficients. The performance of the MFM method is also compared with the single-fidelity metamodeling method using HF samples. Both the approaches produced similar optimal shapes; however, the optimal shape from MFM achieved a minimum objective function value while more closely satisfying the constraint at a computational cost saving of around 41%.

Nomenclature

A	=	Pitching amplitude, [deg]
c	=	Chord length, [-]
c_d	=	Sectional drag coefficient, [-]
$c_{d_{err}}$	=	Estimated error in average drag coefficient, [d.c.]
c_l	=	Sectional lift coefficient, [-]
c_m	=	Sectional pitching moment coefficient, [-]
$c_{d_{RE}}$	=	Richardson extrapolation estimate of average drag coefficient per cycle, [d.c.]
d.c.	=	Drag counts, $\Delta c_d = 0.0001$
Δc_l	=	Change in sectional lift coefficient, [-]
f	=	Scalar objective function
g	=	Inequality constraint function
k_r	=	Reduced frequency
M	=	Freestream Mach number
m_{max}	=	Airfoil maximum camber as percentage of the chord length, [%]

*Ph.D. Student, Department of Aerospace Engineering
†Associate Professor, Department of Aerospace Engineering, AIAA Senior Member.

N	=	Number of time steps in each pitching cycle
n_c	=	Number of low-fidelity design samples
n_e	=	Number of high-fidelity design samples
n_t	=	Number of test data samples
n_s	=	Number of design samples
Re	=	Reynolds number
t_{max}	=	Airfoil maximum thickness as percentage of the chord length, [%]
U	=	Freestream velocity, $[\frac{m}{s}]$
TI	=	Turbulence intensity, [-]
$x_{m_{max}}$	=	Location of maximum camber as percentage of the chord length, [%]
y^+	=	Non-dimensionalized first layer cell thickness
z	=	z-coordinate of airfoil section, [-]
$\mathbf{x}$	=	Design variable vector
$\mathbf{x}_{lb}$	=	Vector containing lower bounds on design variables
$\mathbf{x}_{ub}$	=	Vector containing upper bounds on design variables
α	=	Angle of attack, [deg]
ω	=	Rotational rate, $[\frac{rad}{s}]$
$\Delta\alpha$	=	Delay in dynamic stall angle, [deg]
α_{ds}	=	Dynamic stall angle of attack, [deg]
$\boldsymbol{\theta}$	=	Vector of Kriging hyperparameters
λ	=	Hyperparameter of Kriging regression
ρ	=	Hyperparameter of Cokriging regression

I. Introduction

The phenomenon of dynamic stall is widely observed on the aerodynamic surfaces which are in relative motion to the incoming flow velocity or when they are subjected to unsteady incoming flow with varying direction. Rotorcraft [1] and commercial-grade wind turbines [2] are the two well known high Reynolds number applications where dynamic stall effects are important. At low Reynolds number dynamic stall is observed in vertical axis wind turbines [3, 4] and bio-inspired micro-air vehicles (MAVs)[5]/unmanned air vehicles (UAVs).

The predominant features of dynamic stall are the formation, generation, and shedding of an energetic leading-edge vortex (LEV) or dynamic stall vortex (DSV) over the aerodynamic surface. These characteristics induce fluctuating pressure fields producing a significant transient variation in aerodynamic forces and moments, considerably higher than their static counterparts. The formation of such adverse loading negatively affects structural strength and fatigue life of the system [6, 7], which has inspired designers to improve designs that can mitigate or delay dynamic stall characteristics.

Aerodynamic shape optimization (ASO) provides an effective approach to passively delay and mitigate dynamic stall characteristics without the addition of an auxiliary system. ASO has been widely used in solving steady-state [7], and to some extent, in unsteady aerodynamic problems. ASO usually requires multiple evaluations using time-consuming computational fluid dynamics (CFD) models, which makes it expensive for unsteady problems such as dynamic stall. However, ASO has been steadily gaining interest from multiple researchers [7–11] for dynamic stall delay and mitigation.

ASO studies on dynamic stall delay and mitigation are typically done with adjoint-based CFD simulation [7–9, 12] and have shown promising results. The adjoint-based approach is a modern approach to solve ASO problems [13] providing accelerated optimization search with an efficient calculation of gradient information. Additionally, the adjoint-based method is independent of design variables and could be advantageous for solving high dimensional optimization problems [13]. However, the objective function constructed from computational simulations is often non-differentiable, discontinuous, and inherently noisy, which makes sensitivity information often inaccessibly [14]. Further, the adjoint method is dependant on the high-fidelity (HF) simulation and could get computationally expensive for complex unsteady problems such as dynamic stall.

Metamodel-based optimization (MBO) (also called surrogate-based optimization) [14, 15] is an approach to alleviate the computational burden of costly simulation-based design problems. In MBO, a metamodel (also called a surrogate) of the objective function is constructed using a limited number of the time-consuming simulations. The metamodel is fast to evaluate and can be used with local or global search optimizers. Metamodeling methods consists of data-fit methods and multifidelity methods. The data-fit methods fit a response surface through the evaluated objective function

values at sampled points in design space. Some of the widely used data-fit methods are Kriging [16], polynomial chaos expansions (PCE) [17], and support vector regression [18].

Recently, Tang et al. [19] used Kriging metamodeling technique for shape optimization of cycloidal rotor airfoil in unsteady flow. Wang et al. [20] also successfully applied Kriging method for finding optimal rotor shape for helicopter application. In turbomachinery shape optimization [21–23] MOB approach has also been used successfully where the computational cost of each evaluation can be as high as in dynamic stall CFD simulations.

Data-fit methods typically require large number of HF sample evaluations to obtain accurate metamodel which increases computational cost [24]. Multifidelity modeling techniques [25] can alleviate the computational burden of construction of accurate metamodels using information from multiple fidelities. Multifidelity models (MFM) combine HF and low fidelity (LF) models in an effort to achieve accurate high-fidelity representation at a reasonable cost [24]. The LF models are generally approximations of the HF models and can be obtained using simplified governing equations, changing the discretization of the HF model[24]. Cokriging [26] is a widely known multifidelity modeling technique used in MBO.

In this work, MBO is used for ASO of a generic airfoil at low Reynolds number undergoing deep dynamic stall. In particular, the approach is demonstrated on NACA 0012 airfoil in sinusoidal oscillation with a reduced frequency of 0.05 at Reynolds number of 135,000, and a Mach number of 0.1. The PARSEC airfoil parameterization technique [27] with six design variables is used for generating the airfoil shapes. The airfoil shape evaluation is done using the unsteady Reynolds-averaged Navier-Stokes equations with a C-grid mesh topology and Menter's shear stress transport turbulence model. The multifidelity metamodel is constructed using Cokriging regression [26, 28] and is sequentially refined using the expected improvement [29] infill criteria. The metamodel is validated with the normalized root mean square error (NRMSE) metric. In this work, a multi-start gradient-based search algorithm is used to find the optimum airfoil shapes.

This paper is structured as follows. The next section presents the problem statement for delaying dynamic stall and the setup of the computational model. The following section describes the MBO approach. The result section then follows with detailed results of numerical experiments for the current ASO study. Finally, conclusions and suggestions of future work is described.

II. Problem Statement

This section describes the problem formulation and airfoil parameterization method used in the current study. Further, the CFD modeling is described.

A. Problem formulation

The dynamic stall phenomenon is typically studied with sinusoidal oscillating airfoil in a uniform free-stream flow. The pitching motion of the airfoil is described using the angle of attack as a function of time t given as

$$\alpha(t) = \alpha_m + A\sin(\omega t), \tag{1}$$

where α_m, A, and ω represent the mean angle of attack, amplitude of oscillation, and rotational rate, respectively. The reduced frequency, k_r, is another important parameter and is defined as

$$k_r = \frac{\omega c}{2U}, \tag{2}$$

where c is the airfoil chord length, and U is the free-stream speed. In this work, a deep dynamic stall case from Lee et al. [30] is used. The parameters defining the case are: $\alpha_m = 10°$, $A = 15°$, $k_r = 0.05$, and a Reynolds number of $Re = 135,000$.

The objective of the study is to produce an optimum airfoil shape, which delays the dynamic stall occurrence and mitigate adverse loading over the airfoil. This objective is achieved by delaying the formation of DSV predominantly responsible for sudden divergence in the drag and pitching moment coefficients. The optimization problem is formulated as

$$\min_{\mathbf{x}} \quad f(\mathbf{x}) = \left(\frac{\sum_{i=1}^{N} c_{d_i}(\mathbf{x})}{J(c_{d0})}\right) + \left(\frac{\sum_{i=1}^{N} |c_{m_i}(\mathbf{x})|}{J(c_{m0})}\right) \tag{3}$$

$$s.t. \quad g(\mathbf{x}) = \alpha_{ds0} + \Delta\alpha - \alpha_{ds}(\mathbf{x}) \leq 0 \tag{4}$$

$$\mathbf{x}_{lb} \leq \mathbf{x} \leq \mathbf{x}_{ub} \tag{5}$$

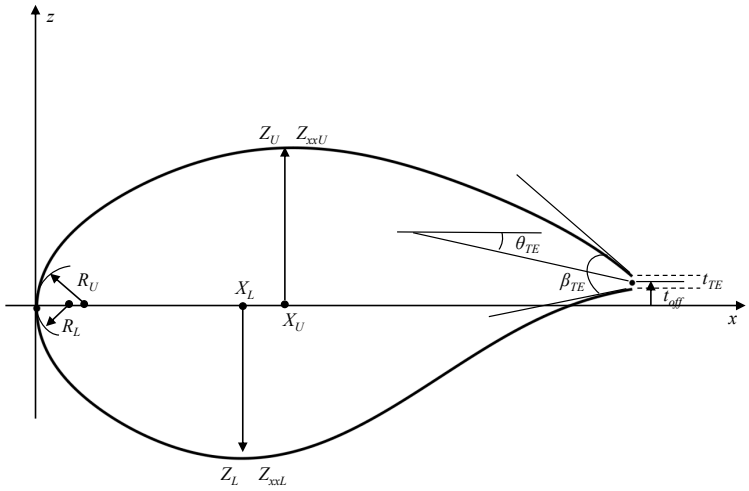

Fig. 1 The PARSEC airfoil geometry parameters

where $J(c_{d0}) = \sum_{i=1}^{N}(c_{d0})_i$, $J(c_{m0}) = \sum_{i=1}^{N}|(c_{m0})_i|$, $\mathbf{x} = [x_1, x_2, \ldots, x_n]^T$ is the design variable vector of n dimensions with $\mathbf{x}_{lb}$ and $\mathbf{x}_{ub}$ as the lower and upper bounds of $\mathbf{x}$, respectively; the parameters $c_d(\mathbf{x})$, $c_m(\mathbf{x})$, and $\alpha_{ds}(\mathbf{x})$ represent time variant drag coefficient, pitching moment coefficient and dynamic stall point of the airfoil shape during pitching cycle, and N denotes the number of timesteps in each pitching cycle. The value of N is depends on simulation timestep and total cycle time. The subscript '0' in (3) and (4) represents the baseline airfoil shape (NACA0012). Parameter $\Delta\alpha$ in (4) denotes the minimum delay in the dynamic stall angle expected in the optimum design, which is set to $\Delta\alpha = 3^\circ$ in this work. For this study, only the upstroke part of the pitching cycle is considered, which is predominantly affected by formation of dynamic stall vortex.

B. Design variables

In this work, the PARSEC [27] parameterization technique is used for describing the airfoil shapes. The PARSEC method offers set of design variables that has a specific meaning and directly controls the airfoil shape characteristics (for e.g. airfoil thickness, leading-edge radius) which could be appealing to designers for understanding effect of shape variables on the dynamic stall characteristics.

PARSEC method involves 12 parameters (Fig. 1) defining the airfoil shape of unit chord. The parameters affecting only the upper surface of the airfoil are considered in this study. Further, the leading edge radius for upper and lower surface are represented by single variable R_{LE}.The trailing edge offset (t_{off}) and thickness (t_{TE}) are set to zero, which generates a sharp trailing edge airfoil (Fig. 1). The above mentioned conditions reduce the 12 design variables to only six variables and the design variable vector is written as

$$\mathbf{x} = [X_U, Z_U, Z_{xx_U}, R_{LE}, \theta_{TE}, \beta_{TE}]^T. \tag{6}$$

The six PARSEC parameters affecting upper surface of airfoil with their respective ranges are shown in Table 1. The subscript 'U' denotes variables for the upper airfoil surface.

C. Computational fluid dynamics modeling

The current study is performed with the Stanford University Unstructured (SU2) unsteady compressible Navier-Stokes (URANS) solver [31]. The dynamic stall simulations are performed using dual time stepping strategy, rigid grid motion and Menter's shear stress transport (SST) turbulence model [32]. The convective fluxes calculated using second-order Jameson-Schmidt-Turkel (JST) scheme [31] and time discretization is done by the Euler implicit scheme [31] with maximum Courant-Friedrichs-Lewy (CFL) number selected as 4 and internal iterations are set to 2,400. The two-level multigrid W-cycle method [31] is also used for convergence acceleration. The Cauchy convergence criteria [33] on

Table 1 Design variables and their bounds for upper airfoil surface

Description	Design variables	Lower bounds	Upper bounds	Units
Upper surface crest x coordinate	X_U	0.2733	0.5011	-
Upper surface crest z coordinate	Z_U	0.054	0.09	-
Second order surface derivative	Z_{xx_U}	-0.6726	-0.4036	-
Leading edge radius	R_{LE}	0.0104	0.0222	-
Trailing edge directional angle	θ_{TE}	-11.7156	-7.0294	deg
Trailing edge wedge angle	β_{TE}	3.52818	5.8803	deg

the drag values is set with Cauchy epsilon as 10^{-6} over last 100 iterations. No-slip boundary condition is used on airfoil surface with farfield condition on external boundary with Reynolds number of 135,000 and Mach number of 0.1. The c-grid mesh is set up an with outer boundary at 55c from airfoil is generated using blockmesh utility provided by OpenFoam [34]. The mesh is refined near the airfoil surface with first layer thickness to obtain $y^+ \leq 0.8$ and growth ratio of 1.05. A low y^+ is necessary to accurately capture the onset of the dynamic stall vortex. Figure 2 shows two views of a coarse version of the mesh used for NACA0012.

The grid and time independence study is done in two steps. Initially, the spatial resolution of the mesh is obtained by conducting grid study on baseline airfoil with steady-state flow condition. The resulting mesh is then used to conduct time study to attain accurate physical timestep for the URANS simulation. The flow and motion parameters are selected from study done by Lee et al. [30] as mentioned in Section II.A. The grid study is done on NACA0012 airfoil at fixed angle of attack $\alpha = 4°$, Re=135,000, and turbulence intensity $TI = 0.08\%$ with SU2 RANS solver. The Cauchy convergence criteria on the drag values is set to a Cauchy-epsilon value of 10^{-6} over 100 flow solver iterations. The maximum solver iterations are set to 150,000. The details of grid study are shown in Table 2. Meshes 2, 3 and 4 show minimal change in lift coefficient $\Delta c_l \leq 0.003$ with the drag counts variation within approximately 4 d.c. Considering the simulation time requirement and accuracy of the results, mesh 2 with 387,000 cells is selected for HF CFD evaluation.

After the selection of appropriate spatial resolution, a time-independent study is conducted to determine the time step required for accurate unsteady simulation of the airfoil pitching cycle. The dynamic stall simulations are conducted with the parameters and flow conditions the same as considered in the experimental study done by Lee et al. [30] (Sec. II.A).

The time step independence study is performed with multiple time steps, as shown in Table 3. The selection of appropriate time step is executed using the generalized Richardson extrapolation method [35] on the average drag

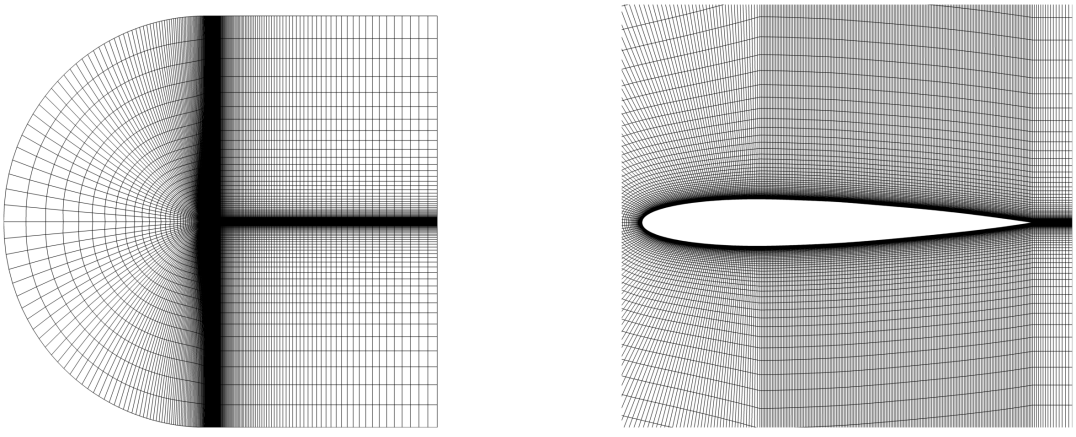

(a) **(b)**

Fig. 2 Coarse mesh with NACA0012 airfoil (a) computational domain, and (b) mesh around the airfoil surface

Table 2 Grid convergence study at Re=135000 and $\alpha = 4°$

Mesh	Number of cells	c_l	c_d (d.c.)	*Simulation time (min)
1	259k	0.395	174.3	75
2	387k	0.414	180.4	146
3	540k	0.416	184.7	220
4	720k	0.417	184.2	298

*Computed on high-performance cluster with 64 processors

Table 3 Time step independence study at $\alpha = 10° + 15° sin(\omega t)$ with $k_r = 0.05$ at $Re = 135,000$

dt (sec)	$c_{d_{avg}}$ (d.c./cycle)	Simulation time* (hrs/cycle)	$c_{d_{err}} = \mid c_{d_{avg}} - c_{d_{RE}} \mid$ (d.c.)
0.004	2,019	51	88.4
0.002	2,093	65	14.9
0.0015	2,103	69	4.8
0.001	2,105	78	2.1
0.0005	2,107	99	0.52

*Computed on a high performance cluster with 112 processors. Wall-clock time.

coefficient per oscillation cycle $c_{d_{avg}}$. Richardson's extrapolation estimate $c_{d_{RE}}$ represents the average drag coefficient per cycle at a lowest possible time step (zero), which is estimated to be $c_{d_{RE}}$ = 2,108 d.c. Table 3 summarizes the results. The simulation time and estimated error $c_{d_{err}}$ from Richardson extrapolation estimate $c_{d_{RE}}$ are considered to select time step of 0.0015 sec for the accurate CFD evaluation of the dynamic stall case. In the current study, all HF model evaluations are conducted with a mesh size of 387,000 cells and a time step of 0.0015 sec.

The LF models are an essential component of multifidelity models as they estimate output response at much lower computational cost with lower accuracy compared to the HF models [25]. In this study, the LF model is generated by simplifying the HF model spatial and temporal discretizations such that the trends in aerodynamic responses are preserved with the least possible computational time requirement. In particular, the LF model is generated with a mesh size of 287,000 cells, time step of 0.004 sec, internal iteration of 1,000, and setting Cauchy convergence criteria on the drag to 10^{-3} over 100 iterations. The constructed LF model reduces simulation time to around 5 hours (wall-clock time) for a complete cycle with the same computational resources used for the HF model.

The aerodynamic response of HF and LF model selected for the current study is compared against the experimental [30] and LES simulation [36] results for NACA0012 airfoil at the selected dynamic stall case and presented in Fig. 3. It should be noted that the presented aerodynamic response from experimental results is the ensemble-average over a hundred cycles [30]. The LES model results by Kim et al. [36] are ensemble-averaged over three cycles, whereas the HF, LF model aerodynamic response are obtained over a single cycle.

From Fig. 3 it is observed that the HF-URANS model show a reasonable agreement with LES and experimental results in upstroke part of cycle, however, the predictions after the dynamic stall occurrence are affected as airfoil moves in the separated flow region. HF-URANS overpredicts peak lift and pitching moment coefficient while underpredicting moment and dynamic stall point. The LES model show a closer agreement with experimental data while HF-URANS show a qualitative agreement with experimental results. The LF-URANS follow a very similar trend as HF-URANS in their aerodynamic responses satisfying similarity requirement of multifidelity modeling methods. Overall, considering the computational time and resource requirement of LES model URANS is a practical option for the dynamic stall evaluation of airfoils for optimization studies.

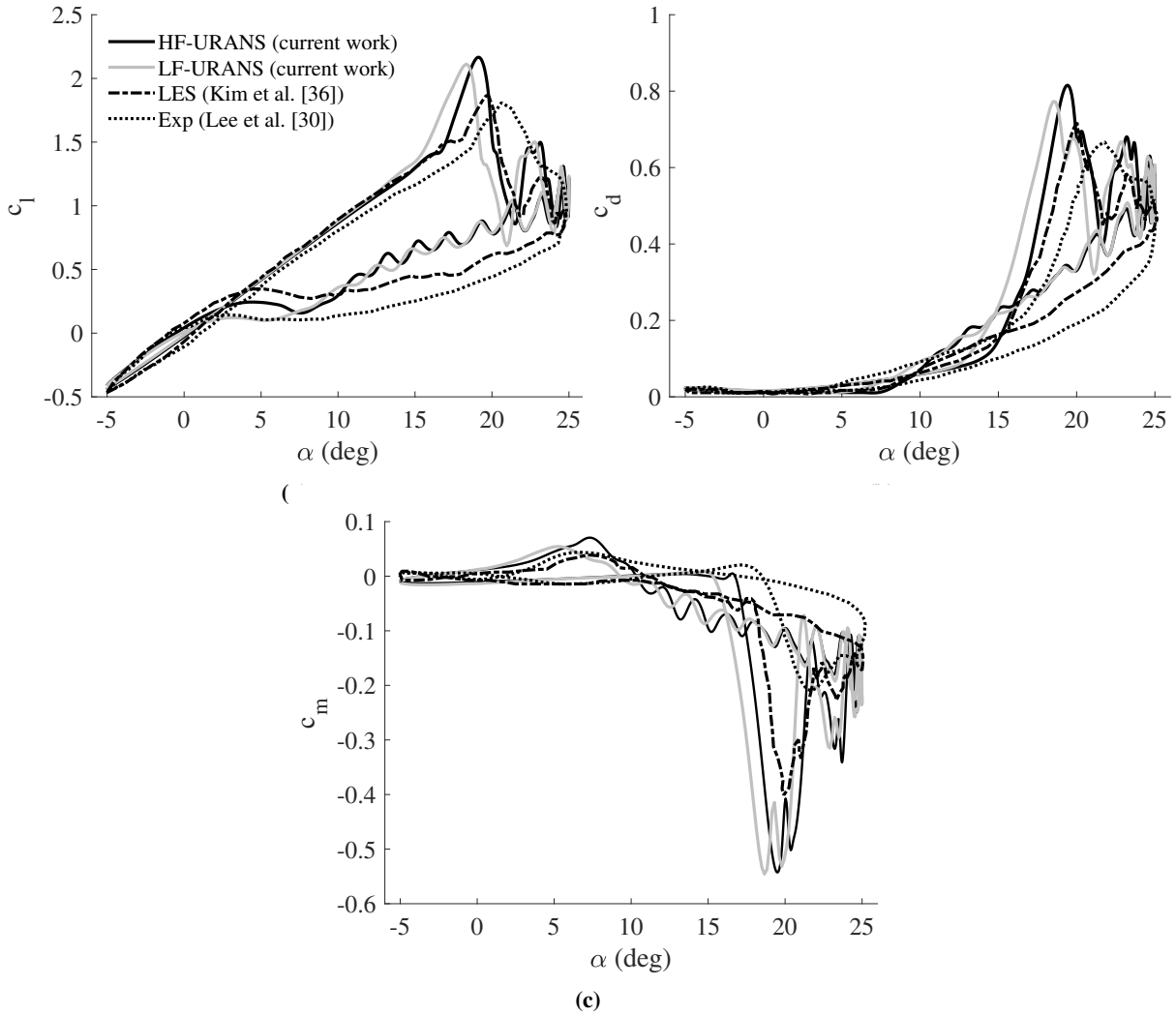

(c)

Fig. 3 A comparison of the time dependent aerodynamic coefficients: (a) lift coefficient, (b) drag coefficient, (c) pitching moment coefficient obtained from the URANS model (current work), LES model [36] and experiments [30] with oscillation cycle parameters $\alpha = 10^\circ + 15^\circ sin(\omega t)$ and $k_r = 0.05$

III. Methods

This section describes the MBO algorithm used to construct the Cokriging regression multifidelity metamodel. In particular, the details of the workflow, sampling plan, Cokriging regression metamodel, infill criteria and validation are described.

A. Workflow

A flowchart of the MBO algorithm is shown in Fig. 4. The algorithm presented in this study is an automated loop that sequentially improves the multifidelity metamodel accuracy. The algorithm starts by sampling the design space with an initial number of points. The LF model is then evaluated at all the design points, whereas the HF model is evaluated at a subset of the initial samples. The design sample evaluation is conducted with the CFD model. The Cokriging regression metamodel is then constructed by combining HF and LF observations. The constructed metamodel is then validated against the test data set. If metamodel does not meet the required criteria, then the expected improvement [29] infill strategy is used to find an infill point in design space, which could improve the accuracy of the model. The above process is continued until the metamodel satisfies the termination criteria. Once the metamodel is sufficiently accurate, the optimum design is found by the application of optimization methods on the constructed metamodel.

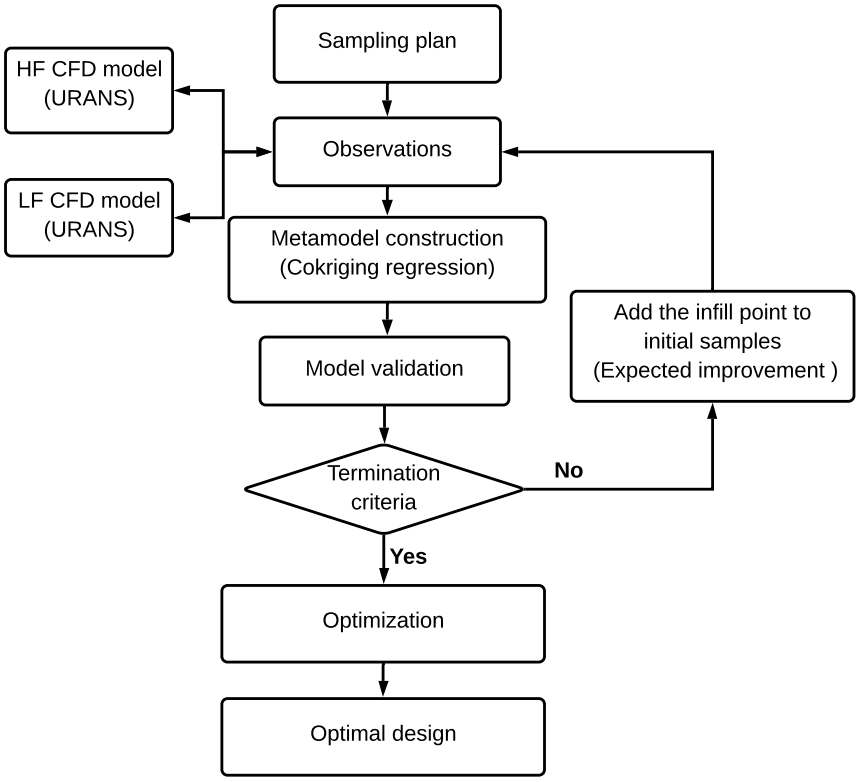

Fig. 4 Flowchart of the metamodel-based optimization algorithm using Cokriging regression

B. Sampling plan

The accurate construction of metamodel starts with an appropriate sampling plan. It is important to capture the trend of the objective function over the entire design domain. The Latin hypercube sampling (LHS) [29, 37] method provides a good distribution of sample points over the design domain, ensuring the entire range of design variables are represented. In this study, the LHS method is used to generate training and testing data samples. The LF model is evaluated on all the training samples, while the HF model is evaluated on a limited subset of training data. Additionally, the HF model is evaluated at all the test data points for the metamodel validation.

C. Cokriging regression

Simulation-based objective functions can be noisy. The objective functions formulated from computational simulations, such as CFD could exhibit noise from numerical modeling [38]. In the current study, the objective function could involve a noise from the CFD evaluation of airfoil dynamic stall in a separated flow region. The Cokriging regression offer a multifidelity approach to extract a smooth trend from the data by filtering noise.

In this study, Cokriging regression [29] is used for aerodynamic shape optimization to delay dynamic stall of an airfoil. Cokriging regression [26, 29] is the two-fidelity version of Kriging regression [29, 38], constructed in a similar manner as Cokriging [26]. The detailed theory behind Cokriging regression can be found in Forrester et al. [26], while the implementation used in this study is based on an algorithm developed by Thelen et al. [39].

A Kriging regression predictor is given as

$$\hat{y}_r(\mathbf{x}) = \mathbf{g}^T \hat{\boldsymbol{\beta}}_r + \mathbf{r}^T \ (\mathbf{R} + \lambda \mathbf{I})^{-1} (\ \mathbf{y} - \mathbf{G}\hat{\boldsymbol{\beta}}_r), \tag{7}$$

where

$$\hat{\boldsymbol{\beta}}_r = \frac{\mathbf{G}^T (\mathbf{R} + \lambda \mathbf{I})^{-1} \mathbf{y}}{\mathbf{G}^T (\mathbf{R} + \lambda \mathbf{I})^{-1} \mathbf{G}}, \tag{8}$$

$$\mathbf{r} = \mathbf{r}(\mathbf{X}, \mathbf{x}) = R(\mathbf{X}, \mathbf{x}), \tag{9}$$

$$\mathbf{R} = \mathbf{R}(\mathbf{X}, \mathbf{X}) = R(\mathbf{X}, \mathbf{X}), \tag{10}$$

and

$$\mathbf{G} = \mathbf{g}(\mathbf{X}). \tag{11}$$

In the equations above, $\mathbf{y}$ is the column vector of observed response at known n_s design samples $\mathbf{X} = [\mathbf{x}^1, \mathbf{x}^2, ..., \mathbf{x}^{n_s}]^T$, $\hat{\boldsymbol{\beta}}_r$ is the maximum likelihood estimate (MLE) [38] of the regression coefficients, $\mathbf{g}$ is the regression basis functions, $\mathbf{R}$ is the correlation matrix between known design samples $\mathbf{X}$, $\mathbf{I}$ is the identity matrix, λ is the scalar hyperparameter which filters noise from the data, and $\mathbf{r}$ is the correlation vector between untried design sample $\mathbf{x}$ and known samples $\mathbf{X}$. The correlation function R used in $\mathbf{R}$ describes the correlation between any two design samples based on the distance using Gaussian basis function given as [38]

$$R(\mathbf{x}^i, \mathbf{x}^j) = \exp\Big[-\sum_{k=1}^{n} \theta_k \left| x_k^i - x_k^j \right|^2 \Big], \tag{12}$$

where θ_k is the k^{th} unknown hyperparameter parameter of $\boldsymbol{\theta} = [\theta_1, \theta_2, ..., \theta_n]^T$, x_k^i and x_k^j are the k^{th} components of any two known samples $\mathbf{x}^i$, $\mathbf{x}^j$ of n design variables from $\mathbf{X}$. The hyperparameters $\boldsymbol{\theta}$ and λ are found by maximizing concentrated ln-likelihood function [29, 38] using numerical optimization. One of the important feature of Kriging regression is the estimation of mean squared error (MSE) at unsampled point which could be used for refining metamodel with infill strategies [29]. The Kriging regression MSE can be estimated as

$$\hat{s}_r^2(\mathbf{x}) = \hat{\sigma}_r^2 \Big[1 + \lambda - \mathbf{r}^T (\mathbf{R} + \lambda \mathbf{I})^{-1} \mathbf{r} + \frac{1 - \mathbf{G}^T (\mathbf{R} + \lambda \mathbf{I})^{-1} \mathbf{r}}{\mathbf{G}^T \mathbf{R}^{-1} \mathbf{G}} \Big], \tag{13}$$

where the estimated Gaussian process variance is given as

$$\hat{\sigma}_r^2 = \frac{(\mathbf{y} - \mathbf{G}\hat{\boldsymbol{\beta}}_r)^T (\mathbf{R} + \lambda \mathbf{I})^{-1} (\mathbf{y} - \mathbf{G}\hat{\boldsymbol{\beta}}_r)}{n_s}. \tag{14}$$

The Cokriging regression model used in this study is a two-fidelity model where the HF response $\mathbf{y}_e$ at $\mathbf{X}_e = [\mathbf{x}_e^1, \mathbf{x}_e^2, ..., \mathbf{x}_e^{n_e}]^T$ points and the LF response $\mathbf{y}_c$ at points $\mathbf{X}_c = [\mathbf{x}_c^1, \mathbf{x}_c^2, ..., \mathbf{x}_c^{n_c}]^T$, where $\mathbf{X}_e \subset \mathbf{X}_c$. Subscript 'c' and 'e' represents cheap and expensive model respectively whereas parameter n_e and n_c represents number of HF and LF samples respectively. The Cokriging regression predictor is created by combining the LF Kriging regression model, $\hat{y}_{c,r}(\mathbf{x})$, and a difference Kriging regression model, $\hat{y}_{d,r}(\mathbf{x})$, and is written as

$$\hat{y}_{e,r}(\mathbf{x}) = \rho \hat{y}_{c,r}(\mathbf{x}) + \hat{y}_{d,r}(\mathbf{x}), \tag{15}$$

where ρ is the hyperparameter that scales the LF approximation to the HF response. Initially, the Kriging regression model is fitted to the LF sample response $\mathbf{y}_c(\mathbf{X}_c)$ to obtain $\hat{y}_{c,r}(\mathbf{x})$, where the hyperparameters $\boldsymbol{\theta}_c$ and λ_c are obtained by maximizing the MLE function. Next, the difference Kriging regression model is fitted to $\mathbf{y}_d(\mathbf{X}_e) = \mathbf{y}_e(\mathbf{X}_e) - \rho \hat{y}_{c,r}(\mathbf{X}_e)$ to obtain $\hat{y}_{d,r}(\mathbf{x})$, where the second set of hyperparameters $\boldsymbol{\theta}_d$, λ_d and ρ are obtained, again by maximizing the MLE function. The Cokriging regression predictor is now written as [39]

$$\hat{y}_{e,r}(\mathbf{x}) = \mathbf{g}^T \hat{\boldsymbol{\beta}} + \mathbf{c}^T \ \mathbf{C}^{-1} (\ \mathbf{y} - \mathbf{G}\hat{\boldsymbol{\beta}}), \tag{16}$$

where

$$\mathbf{C} = \begin{bmatrix} \hat{\sigma}_{c,r}^2 \left\{ \mathbf{R}_c(\mathbf{X}_c, \mathbf{X}_c) + \mathbf{I}_{(n_c \times n_c)} \lambda_c \right\} & \rho\ \hat{\sigma}_{c,r}^2 \left\{ \mathbf{R}_c(\mathbf{X}_c, \mathbf{X}_e) + \begin{bmatrix} \mathbf{0}_{(n_c - n_e \times n_e)} \\ \mathbf{I}_{(n_e \times n_e)} \end{bmatrix} \lambda_c \right\} \\ \rho\ \hat{\sigma}_{c,r}^2 \left\{ \mathbf{R}_c(\mathbf{X}_e, \mathbf{X}_c) + \left[\mathbf{0}_{(n_e \times n_c - n_e)} \mathbf{I}_{(n_e \times n_e)} \lambda_c \right] \right\} & \rho^2\ \hat{\sigma}_{c,r}^2 \left\{ \mathbf{R}_c(\mathbf{X}_e, \mathbf{X}_e) + \mathbf{I}_{(n_e \times n_e)} \lambda_c \right\} \\ & + \hat{\sigma}_{d,r}^2 \left\{ \mathbf{R}_d(\mathbf{X}_e, \mathbf{X}_e) + \mathbf{I}_{(n_e \times n_e)} \lambda_d \right\} \end{bmatrix}, \tag{17}$$

$$\mathbf{c} = \begin{bmatrix} \rho\ \hat{\sigma}_{c,r}^2\ \mathbf{r}_c(\mathbf{X}_c, \mathbf{x}) \\ \rho^2\ \hat{\sigma}_{c,r}^2\ \mathbf{r}_c(\mathbf{X}_e, \mathbf{x}) + \hat{\sigma}_{d,r}^2\ \mathbf{r}_d(\mathbf{X}_e, \mathbf{x}) \end{bmatrix}, \tag{18}$$

$$\mathbf{G} = \begin{bmatrix} \mathbf{g}(\mathbf{X}_c) \\ \mathbf{g}(\mathbf{X}_e) \end{bmatrix}. \tag{19}$$

$$\mathbf{y} = \begin{bmatrix} \mathbf{y}(\mathbf{X}_c) \\ \mathbf{y}(\mathbf{X}_e) \end{bmatrix}, \tag{20}$$

and

$$\hat{\boldsymbol{\beta}} = \hat{\boldsymbol{\beta}}_{c,r} + \hat{\boldsymbol{\beta}}_{d,r}. \tag{21}$$

Here, $\mathbf{C}$ is the covariance matrix between the known LF ($\mathbf{X}_c$) and HF samples ($\mathbf{X}_e$), $\mathbf{I}$ is an identity matrix, $\mathbf{0}$ is a zero matrix, $\mathbf{c}$ is the covariance vector between known samples and untried point $\mathbf{x}$, $\mathbf{y}$ is the vector containing the LF and HF observed response, $\mathbf{G}$ is a regression basis function at $\mathbf{X}_c$ and $\mathbf{X}_e$, and $\hat{\boldsymbol{\beta}}$ is the regression coefficient given as the sum of LF $\hat{\boldsymbol{\beta}}_{c,r}$ and difference $\hat{\boldsymbol{\beta}}_{d,r}$ model regression coefficients each obtained using (8). In the equations above, Gaussian variances $\hat{\sigma}^2_{c,r}$ and $\hat{\sigma}^2_{d,r}$ are obtained using (14). Similar to Kriging regression, the Cokriging regression estimated MSE can be given as [39]

$$\hat{s}^2_r(\mathbf{x}) = \rho^2 \hat{\sigma}^2_{c,r}(1+\lambda_c) + \hat{\sigma}^2_{d,r}(1+\lambda_d) - \mathbf{c}^T\mathbf{C}^{-1}\mathbf{c} + \frac{1 - \mathbf{G}^T\mathbf{C}^{-1}\mathbf{c}}{\mathbf{G}^T\mathbf{C}^{-1}\,\mathbf{G}}. \tag{22}$$

D. Infill criteria

The metamodels are the approximation of the true function response and based on the sample data available for the training process. The optimum design depends on the accuracy of the model, thus it is advisable to improve accuracy of the metamodel by addition of infill points to the initial samples. In this study, the expected improvement (EI) infill criteria [29] is used for a balanced exploration and exploitation of the design space. The EI function for Gaussian process models is written as

$$\mathbb{E}[I(\mathbf{x})] = \begin{cases} (y_{\min} - \hat{y})\ \Phi\left(\frac{y_{\min}-\hat{y}}{\hat{s}}\right) + \hat{s}\ \phi\left(\frac{y_{\min}-\hat{y}}{\hat{s}}\right) & \text{when } \hat{s} > 0 \\ 0 & \text{when } \hat{s} = 0 \end{cases} \tag{23}$$

where $\hat{y}$ and $\hat{s}$ are the metamodel predictor and the MSE estimate, respectively, Φ is the normal cumulative distribution function, ϕ is the normal probability density function, and y_{min} is the minimum observed response from the training data. The EI function (23) can be implemented as

$$\mathbb{E}[I(\mathbf{x})] = (y_{\min} - \hat{y})\ \left[\frac{1}{2} + \frac{1}{2}\ \text{erf}\left(\frac{y_{\min} - \hat{y}}{\hat{s}\sqrt{2}}\right)\right] + \hat{s}\frac{1}{2\pi}\ \exp\left[\frac{-(y_{\min} - \hat{y})^2}{\hat{s}}\right], \tag{24}$$

where 'erf' is the error function and is defined as

$$\text{erf}(z) = \frac{2}{\sqrt{\pi}} \int_0^z e^{-t^2}\, dt. \tag{25}$$

The infill point from the trained metamodel is determined by maximizing the EI function (24) with a global optimizer.

It should be noted that Kriging regression or Cokriging regression should not be directly used with the EI approach because of the possibility of resampling at already observed locations, thereby halting convergence [29]. Thus, to resolve resampling at existing location Kriging regression MSE ($\hat{s}^2_r$) in (13) is redefined using a re-interpolation approach [26, 38] where the computation of $\hat{\sigma}^2_r$ in (14) is replaced with $\hat{\sigma}^2_{ri}$ and given as

$$\hat{\sigma}^2_{ri} = \frac{(\mathbf{y} - \mathbf{G}\hat{\beta}_r)^T\,(\mathbf{R} + \lambda\mathbf{I})^{-1}\,\mathbf{R}\,(\mathbf{R} + \lambda\mathbf{I})^{-1}(\mathbf{y} - \mathbf{G}\hat{\beta}_r)}{n_s}. \tag{26}$$

The subscript 'ri' in (26) represents re-interpolation. The EI infill criteria accompanied by re-interpolation can be used with Cokriging regression where computation of Gaussain process variance $\hat{\sigma}^2_{c,r}$ and $\hat{\sigma}^2_{d,r}$ in (22) are replaced with $\hat{\sigma}^2_{c,ri}$ and $\hat{\sigma}^2_{d,ri}$ using (26).

E. Validation

The global accuracy of the metamodel is measured using the normalized root mean squared error (NRMSE) and is defined as

$$\text{NRMSE} = \frac{\sqrt{\sum_{i=1}^{n_t} \frac{(y_t^i - \hat{y}_t^i)^2}{n_t}}}{(y_{\max} - y_{\min})_t}, \tag{27}$$

where y_t^i and $\hat{y}_t^i$ represent response of from HF CFD evaluation and metamodel estimation at i^{th} test samples, respectively. The response value y_t denotes objective function $f(\mathbf{x})$ or constraint function $g(\mathbf{x})$ values for their respective error estimation. The n_t indicates the number of test data samples. The denominator of $(y_{\max} - y_{\min})_t$ represents the difference of the maximum and minimum responses from the test data samples. For this study, a separate test dataset is generated using a LHS sampling plan.

IV. Results

The proposed MBO algorithm discussed in this work is demonstrated initially on an analytical problem and then on a deep dynamic stall case. The analytical problem is a one-dimensional multifidelity test case presented by Forrester et al. [29], where different level of noise is added to the HF and LF functions. In the next section, the proposed algorithm is applied for delaying the dynamic stall over an airfoil. First, the details of metamodel construction, infill process, and metamodel accuracy are presented. Then, the optimal design and its dynamic stall characteristics are presented. The optimum shape from the current approach is also compared against baseline design and the optimum shape obtained from the author's previous work [40] using Kriging regression.

A. Analytical function

The proposed optimization algorithm using Cokriging regression (CKR) with expected improvement infill criteria is demonstrated on a one dimensional analytical function. The high- and low-fidelity analytical functions are [29]

$$f_e(x) = (6x - 2)^2 sin(12x - 4) + N(0, 0.5), \tag{28}$$

and

$$f_c(x) = A f_e + B(x - 0.5) - C + N(0, 0.25), \tag{29}$$

respectively, where $x \in [0, 1]$, and A, B, and C are 0.4, 10, and 10, respectively. A normally distributed random noise with a mean zero is added to the functions f_e and f_c with a standard deviation of 0.5 and 0.1, respectively. The subscript 'e' and 'c' in (28) and (29) represent the HF and LF analytical functions. The goal of this case is to model the noisy HF analytical function (f_e) approximately and locate a global minimum near $x^* \approx 0.76$.

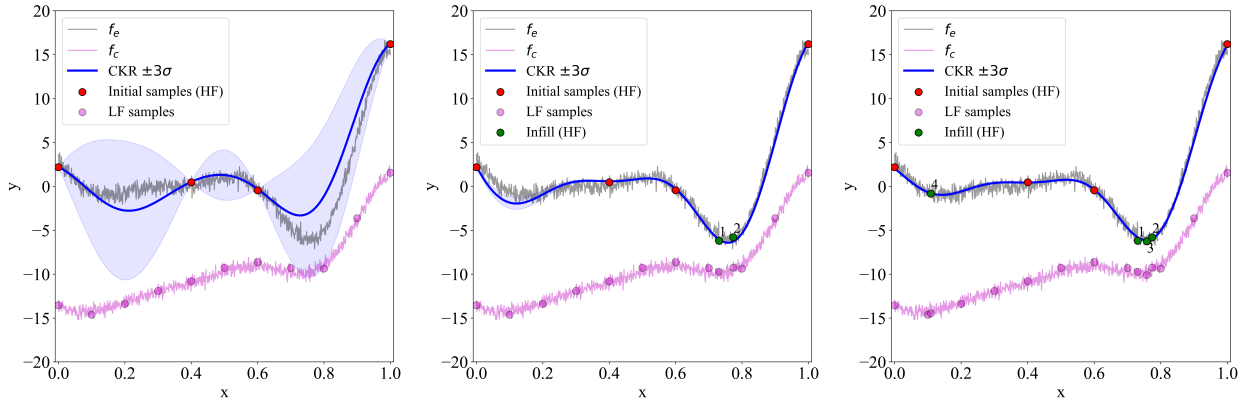

(a) **(b)** **(c)**

Fig. 5 Cokriging regression (CKR) with EI infill criteria on the one-dimensional analytical function (a) initial metamodel, (b) with two infill points, and (c) with four infill points

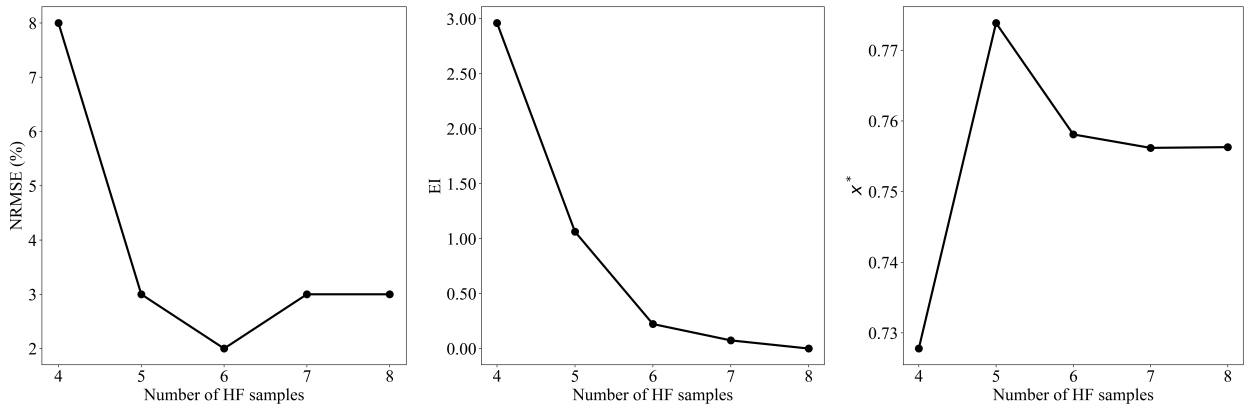

(a) **(b)** **(c)**

Fig. 6 Progression of NRMSE, EI, and the optimum of the one-dimensional analytical problem

Figure 5 shows the progression of the CKR model approximation with the addition of infill points using EI criteria with re-interpolation. The initial sampling plan includes 4 HF samples (n_e) and 11 LF samples (n_c) (Fig. 5a). A new infill point is determined in each iteration and added to the HF and LF initial sampling plan. It should be noted that the error at already sample points goes to zero with re-interpolation while the CKR model regresses through available data as seen in Fig. 5.

Figure 6 show the convergence history of the NRMSE error, maximum EI magnitude, and predicted optimum of the metamodel. For the analytical problem a stopping criteria based on magnitude of maximum EI ($\max(\text{EI}) = 0$) is considered. From Figs. 5 and 6 it is seen that the trained CKR model provides an approximate representation of the HF function.

B. Dynamic stall case

1. Metamodel construction

The proposed MBO algorithm is applied for delaying dynamic stall occurrence over an airfoil. The selection of HF and LF model samples (n_e and n_s) in a one-dimensional case is much easier compared to the high dimensional dynamic stall case (6 dimensions). The LF simulation model considered in this study is significantly cheaper than the HF one, which takes around 3 hours to complete the upstroke cycle, while the HF simulation model takes around 40 hours. Thus, the LF model is generously used to provide a global low-fidelity approximation. A conservative number of HF samples are used to construct CKR metamodel. For this study, a total of 220 LF and 20 HF samples are used for the initial construction of the CKR metamodel. Two separate CKR metamodels are constructed, one for the objective function and the other for the constraint function. The constructed metamodels are validated against 20 test data points generated using the LHS plan and evaluated using high- and low-fidelity CFD simulation model. In this study, the NRMSE metric is used for the validation of CKR metamodels. Similarly, low-fidelity (LF) KR models ($\hat{y}_{c,r}$) used for the construction of the CKR model are also validated with NRMSE metric using LF test data evaluations. A termination criteria of NRMSE $\leq$ 10% on CKR model of the objective function or a fixed budget of 10 infills samples is used in this study. The infill points are determined based on the CKR model of the objective function using EI criteria. Each infill point is evaluated using HF and LF CFD simulation model and added to their respective initial samples to sequentially refine metamodels.

Figure 7 shows the NRMSE metric for objective and constraint function metamodels. The CKR model of objective and constraint function are shown in Fig. 7a. It is observed that after the addition of 10 infill points, the CKR model of the constraint function shows higher accuracy than the CKR model of the objective function, reaching NRMSE of 7.7% and 23.3%, respectively. The CKR model of objective function does not satisfy accuracy criteria (NRMSE $\leq$ 10%), indicating a need for additional high-fidelity infill points for improved global accuracy.

The CKR model is constructed using LF KR model (LF-KR), and its accuracy depends on the global accuracy of the LF-KR model. Figure 7b shows the NRMSE metric of the KR model of objective and constraint functions. The LF-KR and CKR model shows similar trend in NRMSE metric. The NRMSE metric of objective function LF-KR model

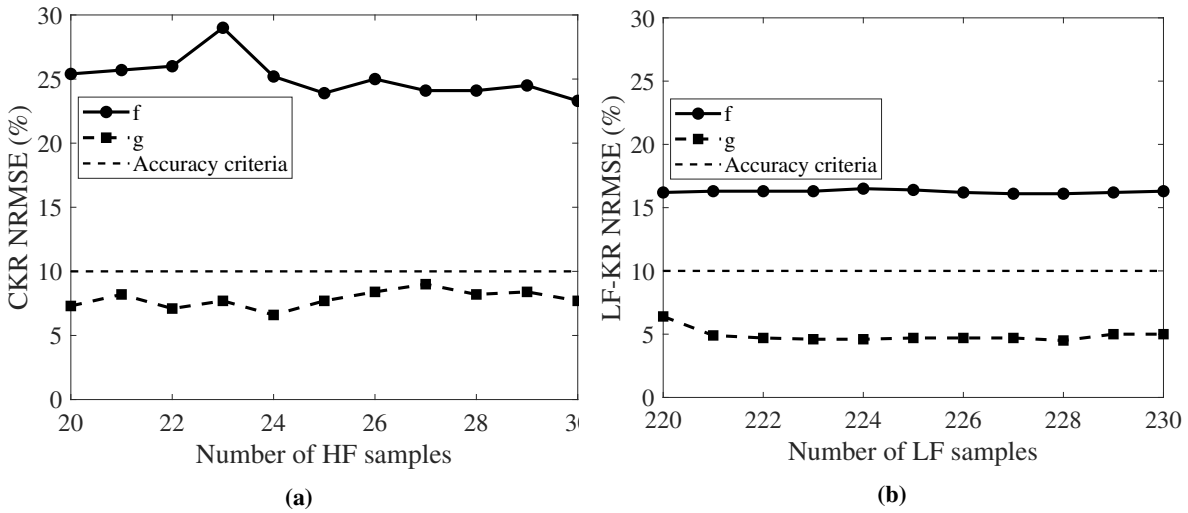

Fig. 7 Metamodel model construction of the objective (f) and constraint (g) functions (a) CKR model validation (b) LF-KR model validation.

does not show much variation, reaching NRMSE of 16.3% at the end of 10 infill points (i.e. with 230 LF samples). Furthermore, the constraint function LF-KR model shows a higher accuracy than the objective function model reaching NRMSE of 5% at the end of 10 infill points. More sampling is needed to improve the global accuracy of LF-KR objective function model. A possible solution would be to add LF samples using exploration-based infill strategy until an accurate LF-KR model is acquired [29].

2. Optimal design

Once the optimization algorithm satisfies the termination criteria the CKR metamodel is passed to the optimizer to find an optimal design using the problem formulation proposed in Sec. II. In this work, a multi-start gradient-based search algorithm is used to find the optimal design. The sequential least squares programming (SLSQP) [41] algorithm offered by the SciPy [42] python package along with 200 starting points generated using LHS sampling are utilized for the optimization process.The best obtained result is realized as the optimal design.

Figure 8a shows the evolution of the optimal shapes after every infill point. The optimum shapes are numbered based on the number HF samples used for construction of CKR model. Only a small variation in consecutive shapes is observed (Fig. 8a). Similar trend is seen from Fig. 8b, which shows the normalized Euclidean distance between the consecutive optimum shapes. The normalized distance is calculated using the z coordinates of the consecutive optimum shapes and normalized with the L2 norm between first two optimum shapes ('opt-21' and 'opt-20'). The normalized Euclidean distance converges from initial optimum. However, the small fluctuations in the normalized Euclidean distance (Fig. 8b) indicate that the optimal design is not completely converged and additional infill points may be required. Nonetheless, the optimal design obtained with 30 HF and 230 LF samples is taken as the optimum airfoil shape for this study.

The optimum shape acquired using the CKR model is compared with the baseline design, as shown in Fig. 9a. Additionally, the current optimum shape is compared with the optimum shape obtained from the study done by Raul et al. [40] using Kriging regression with the high-fidelity data set for the same problem formulation and denoted as 'HF-KR' in this study. The HF-KR investigation used 60 HF samples with 20 infill points added using EI infill criteria producing objective and constraint function metamodel each with less than or equal to 10% NRMSE.

Table 4 provides the airfoil shape details of baseline and optimized designs. The optimized designs show significant variations in shape compared to the baseline. Both the optimized airfoil shapes have a larger leading-edge radius, higher thickness, and camber than the baseline airfoil (Fig. 9a). The optimized shapes obtained from CKR and HF-KR produce similar shapes; however, subtle variations in shapes are seen in Fig. 9a and Table 4. In particular, the optimized shape obtained with the CKR model has a higher maximum thickness of $t_{max} = 15\%$, whereas the higher maximum camber of $m_{max} = 1.89\%$ is observed in an optimized shape obtained from HF-KR model. Interestingly, both the optimum shapes show an aft camber with maximum camber located between $50\% - 65\%$ of the chord length.

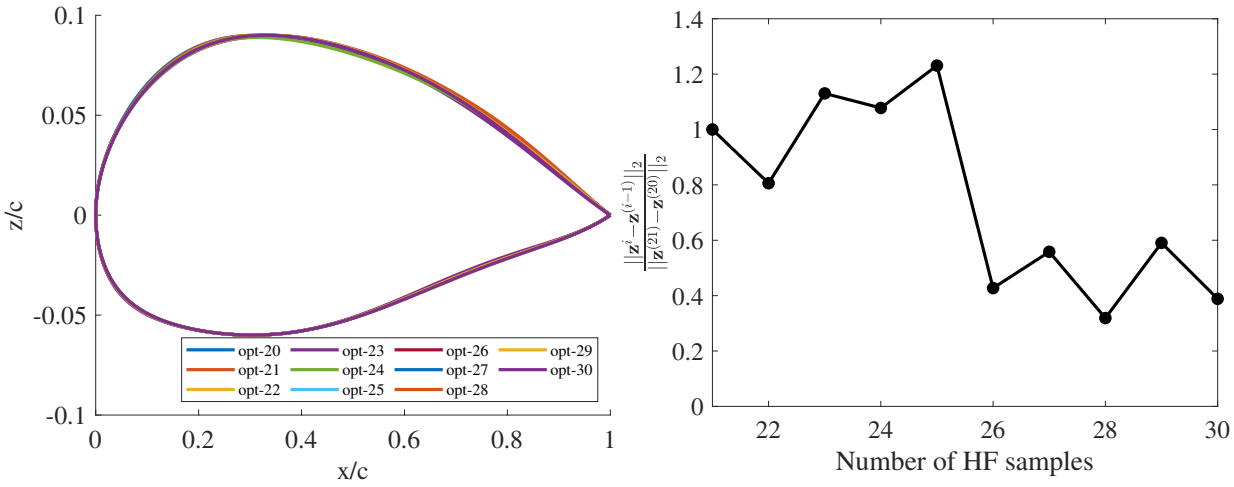

Fig. 8 Evolution of the optimal airfoil shapes: (a) the optimum shapes at the initial surrogate model and at every infill points, and (b) change in z-coordinates of the consecutive optimum designs

The performance of optimum shapes are evaluated using high-fidelity CFD simulation model and their respective aerodynamic characteristics are shown in Fig. 9 along with baseline results for the upstroke pitching cycle. The lift, drag and pitching moment coefficients of the optimized designs shows a delayed dynamic stall when compared to the baseline airfoil. Table 5 gives the details of the dynamic stall characteristics for the optimized and the baseline designs along with their respective objective and constraint function values. Figures 9b and 9c show the delay in formation of DSV, indicated by divergence in drag and pitching moment polar. Both the optimized design delays the dynamic stall to around 22.4° (more than 3° delay) and moment stall to 21.5°. Additionally, the peak pitching moments are reduced in both optimized designs.

Figures 10 and 11 show the vorticity plots of baseline and optimized airfoil obtained from CKR model near the moment and dynamic stall angles presented in Table 5. It can be observed that near the moment stall (16.5°) and dynamic stall (19.1°) point of the baseline airfoil, the optimized shape (optimum from CKR) does not show a formation of DSV (Figs. 10a, 10b, 11a, and 11b). After the angle of attack of 19.1° the baseline airfoil goes in massive separation and sheds secondary vortex (Figs. 10c and 10d). The DSV formation and shedding over the optimized airfoil can be seen from Figs. 11c and 11d.

Overall, both the optimized designs produce a similar delay in dynamic and moment stall compared to the baseline. However, when the objective $f(\mathbf{x})$ and constraint function $g(\mathbf{x})$ magnitudes are compared, the optimized shape produced

Table 4 Properties of the baseline and the optimum airfoil design shapes.

Airfoil shapes	t_{max}	m_{max}	$x_{m_{max}}$
Baseline	12	0	0
Optimum (HF-KR) [40]	14.7	1.89	62.0
Optimum (CKR)	15.0	1.56	52.4

Note: Shape properties are represented as percentage of the chord length

Table 5 Details of dynamic stall cycle

Airfoil	α_{ds}	α_{ms}	$c_{l_{max}}$	$f(\mathbf{x})$	$g(\mathbf{x})$
Baseline (NACA0012)	19.1°	16.5°	2.2	2	-3
Optimum (HF-KR)	22.5°	21.5°	1.8	1.78	-0.37
Optimum (CKR)	22.4°	21.5°	1.6	1.61	-0.24

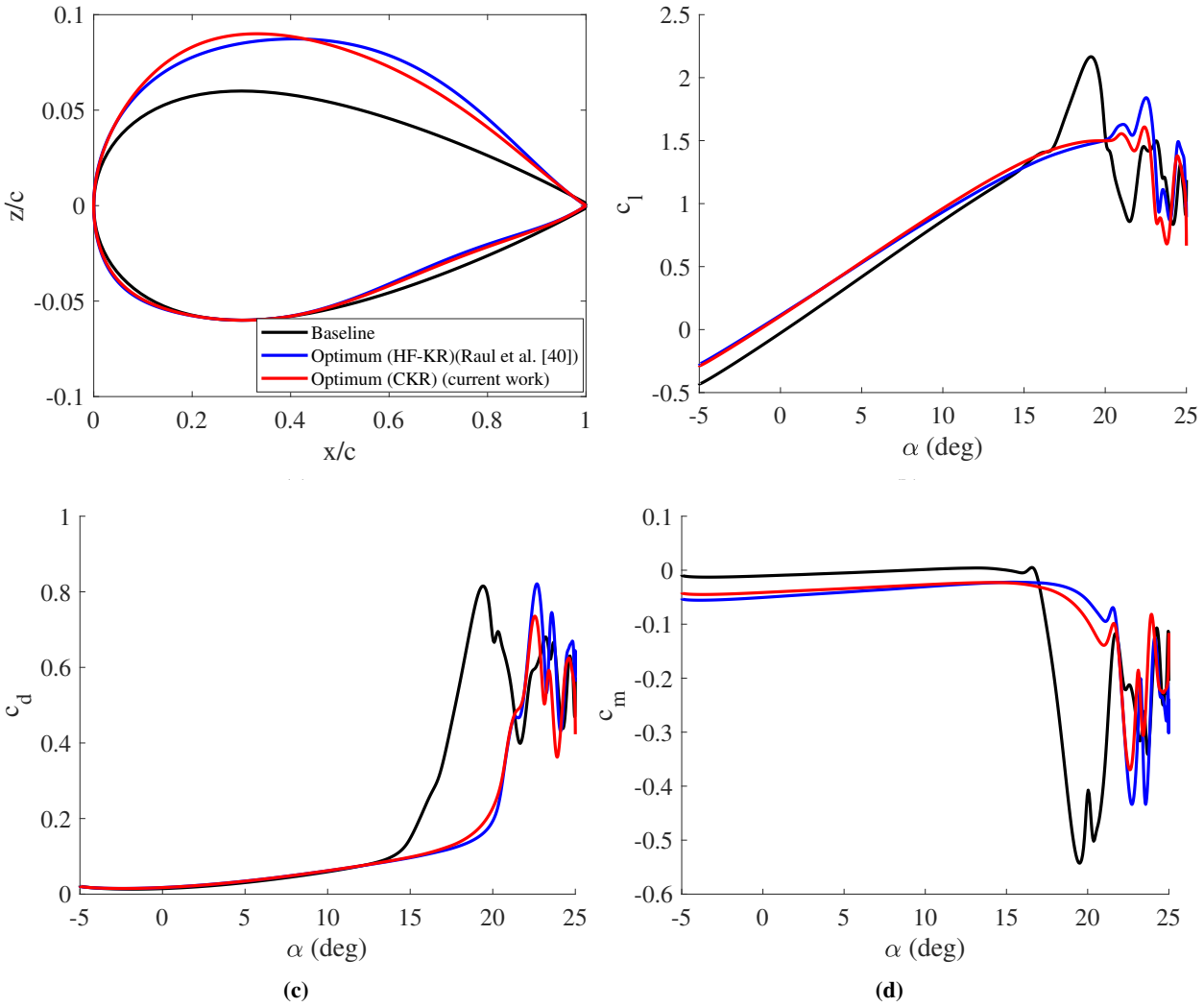

Fig. 9 A comparison of the baseline and optimized designs: (a) airfoil shapes, (b) lift coefficient, (c) drag coefficient, and (d) pitching moment coefficient.

from the CKR model shows a better design for the current problem formulation with a minimum objective function value of 1.61 and more closely satisfying the constraints (Table 5).

In the current study, each high-fidelity CFD evaluation takes around 4,480 CPU hours, whereas the low-fidelity CFD evaluation takes around 336 CPU hours. The entire CKR-based optimization algorithm needs approximately 211,680 CPU hours, considering the negligible cost for training the metamodels. An optimization algorithm with the HF-KR model takes around 358,400 CPU hours producing an accurate metamodel (NRMSE $\leq$ 10%), which is around 13% more accurate than with CKR. However, the current investigation shows that a less accurate multifidelity metamodel could produce optimal design while saving around 41% in computational cost.

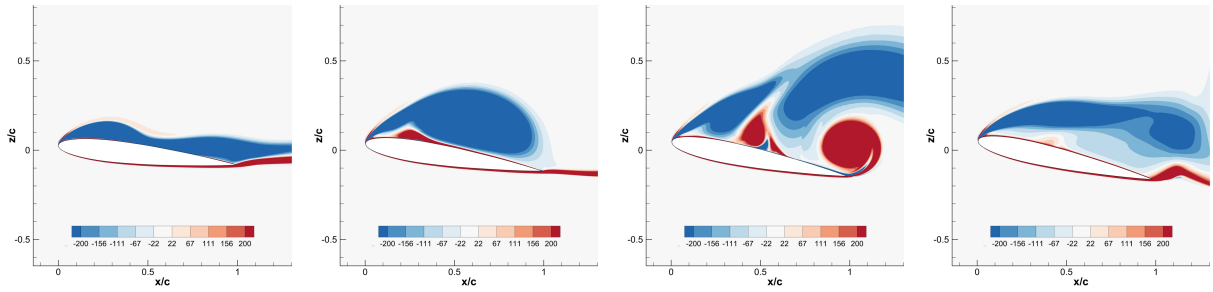

(a) **(b)** **(c)** **(d)**

Fig. 10 Vorticity contour plot of the baseline at (a) $\alpha = 16.3°$, (b) $\alpha = 18.9°$, (c) $\alpha = 21.2°$, and (d) $\alpha = 22.6°$.

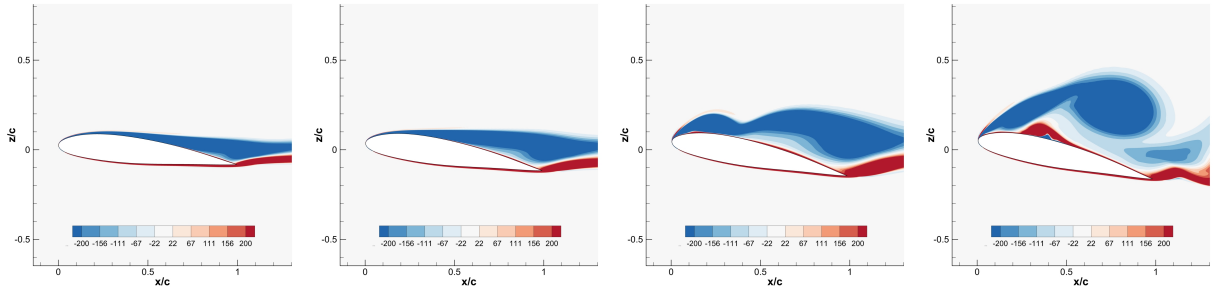

(a) **(b)** **(c)** **(d)**

Fig. 11 Vorticity contour plot of the optimized airfoil from the CKR model at (a) $\alpha = 16.3°$, (b) $\alpha = 18.9°$, (c) $\alpha = 21.2°$, and (d) $\alpha = 22.6°$.

V. Conclusion

In this work, the multifidelity modeling technique is proposed to efficiently delay dynamic stall over the airfoil surface through aerodynamic shape optimization. In particular, the Cokriging regression technique is used to construct a multifidelity metamodel capable of extracting a smooth trend from the data by filtering noise. A conservative number of high-fidelity samples and a generous number of low-fidelity samples are utilized to construct the metamodel for keeping the computational cost low.

The optimal airfoil shape obtained through the proposed approach shows a larger leading-edge radius, a higher maximum thickness, and an increased aft camber when compared to the baseline. Post-optimality analysis shows that the optimal shape significantly delays the dynamic stall and reduces peak lift, drag, and pitching moment coefficients. Further, the formation of a dynamic stall vortex is delayed compared to the baseline design. The performance of the optimized shape is compared with the optimal shape acquired using single-fidelity Kriging regression based on high-fidelity samples. It is observed that Cokriging regression is able to find a better optimal design when compared to Kriging regression by minimizing the objective function and more closely satisfying the constraint of the current problem formulation while saving 41% in computational cost.

In future work, the Cokriging regression model will be further investigated for improving its global accuracy using various exploration based infill strategies while employing the minimum number of high- and low-fidelity samples. Additionally, multiple low-fidelity CFD simulation models will be tested using Cokriging regression to alleviate the computational costs further.

Acknowledgements

This material is based upon work supported by the National Science Foundation under grant no. 1739551.

References

[1] Harris, F. D., and Pruyn, R. R., "Blade Stall Half Fact, Half Fiction," *Journal of the American Helicopter Society*, Vol. 13, No. 2, 1968, pp. 27–48.

[2] Butterfield, C., Simms, D., Scott, G., and Hansen, A., "Dynamic stall on wind turbine blades," Tech. rep., National Renewable Energy Lab., Golden, CO (United States), 1991.

[3] Buchner, A., Lohry, M., Martinelli, L., Soria, J., and Smits, A., "Dynamic stall in vertical axis wind turbines: comparing experiments and computations," *Journal of Wind Engineering and Industrial Aerodynamics*, Vol. 146, 2015, pp. 163–171.

[4] Wang, S., Ingham, D. B., Ma, L., Pourkashanian, M., and Tao, Z., "Numerical investigations on dynamic stall of low Reynolds number flow around oscillating airfoils," *Computers & Fluids*, Vol. 39, No. 9, 2010, pp. 1529–1541.

[5] Ellington, C. P., "The novel aerodynamics of insect flight: applications to micro-air vehicles," *Journal of Experimental Biology*, Vol. 202, No. 23, 1999, pp. 3439–3448.

[6] Carr, L. W., "Progress in analysis and prediction of dynamic stall," *Journal of Aircraft*, Vol. 25, No. 1, 1988, pp. 6–17.

[7] Mani, K., Lockwood, B. A., and Mavriplis, D. J., "Adjoint-based unsteady airfoil design optimization with application to dynamic stall," *American Helicopter Society 68th annual forum proceedings*, Vol. 68, American Helicopter Society, Washington, DC, 2012.

[8] Wong, T., O Malley, J., and O Brien, D., "Investigation of Effect of Dynamic Stall and its Alleviation on Helicopter Performance and Loads," *Annual Forum Proceedings-American Helicopter Society*, Vol. 62-3, 2006, p. 1749.

[9] Nadarajah, S. K., and Jameson, A., "Optimum shape design for unsteady flows with time-accurate continuous and discrete adjoint method," *AIAA Journal*, Vol. 45, No. 7, 2007, pp. 1478–1491.

[10] Wang, Q., Zhao, Q., and Wu, Q., "Aerodynamic shape optimization for alleviating dynamic stall characteristics of helicopter rotor airfoil," *Chinese Journal of Aeronautics*, Vol. 28, No. 2, 2015, pp. 346–356.

[11] Wang, Q., and Zhao, Q., "Rotor airfoil profile optimization for alleviating dynamic stall characteristics," *Aerospace Science and Technology*, Vol. 72, 2018, pp. 502–515.

[12] Economon, T., Palacios, F., and Alonso, J., "Unsteady aerodynamic design on unstructured meshes with sliding interfaces," *51st AIAA Aerospace Sciences Meeting Including the New Horizons Forum and Aerospace Exposition*, Grapevine (Dallas/Ft. Worth Region), Texas, January, 2013, p. 632.

[13] Laurenceau, J., and Meaux, M., "Comparison of gradient and response surface based optimization frameworks using adjoint method," *49th AIAA/ASME/ASCE/AHS/ASC Structures, Structural Dynamics, and Materials Conference, 16th AIAA/ASME/AHS Adaptive Structures Conference, 10th AIAA Non-Deterministic Approaches Conference, 9th AIAA Gossamer Spacecraft Forum, 4th AIAA Multidisciplinary Design Optimization Specialists Conference*, Schaumburg, IL, 2008, p. 1889.

[14] Koziel, S., and Yang, X.-S., *Computational optimization, methods and algorithms*, Vol. 356, Springer, Berlin, Heidelberg, 2011.

[15] Forrester, A. I., and Keane, A. J., "Recent advances in surrogate-based optimization," *Progress in Aerospace Sciences*, Vol. 45, No. 1-3, 2009, pp. 50–79.

[16] Simpson, T. W., Poplinski, J., Koch, P. N., and Allen, J. K., "Metamodels for computer-based engineering design: survey and recommendations," *Engineering with Computers*, Vol. 17, No. 2, 2001, pp. 129–150.

[17] Blatman, G., "Adaptive sparse polynomial chaos expansions for uncertainty propagation and sensitivity analysis," Ph.D. thesis, Université Blaise Pascal, Clermont-Ferrand, 2009.

[18] Smola, A. J., and Schölkopf, B., "A tutorial on support vector regression," *Statistics and Computing*, Vol. 14, No. 3, 2004, pp. 199–222.

[19] Tang, J., Hu, Y., Song, B., and Yang, H., "Unsteady Aerodynamic Optimization of Airfoil for Cycloidal Propellers Based on Surrogate Model," *Journal of Aircraft*, Vol. 54, No. 4, 2017, pp. 1241–1256.

[20] Wang, Q., and Zhao, Q., "Rotor blade aerodynamic shape optimization based on high-efficient optimization method," *Proceedings of the Institution of Mechanical Engineers, Part G: Journal of Aerospace Engineering*, Vol. 234, No. 2, 2020, pp. 375–387.

[21] Khalfallah, S., Ghenaiet, A., Benini, E., and Bedon, G., "Surrogate-based shape optimization of stall margin and efficiency of a centrifugal compressor," *Journal of Propulsion and Power*, Vol. 31, No. 6, 2015, pp. 1607–1620.

[22] Samad, A., Kim, K.-Y., Goel, T., Haftka, R. T., and Shyy, W., "Multiple surrogate modeling for axial compressor blade shape optimization," *Journal of Propulsion and Power*, Vol. 24, No. 2, 2008, pp. 301–310.

[23] Persico, G., Romei, A., Dossena, V., and Gaetani, P., "Impact of shape-optimization on the unsteady aerodynamics and performance of a centrifugal turbine for ORC applications," *Energy*, Vol. 165, 2018, pp. 2–11.

[24] Fernández-Godino, M. G., Park, C., Kim, N.-H., and Haftka, R. T., "Review of multi-fidelity models," *arXiv preprint arXiv:1609.07196*, 2016.

[25] Peherstorfer, B., Willcox, K., and Gunzburger, M., "Survey of multifidelity methods in uncertainty propagation, inference, and optimization," *SIAM Review*, Vol. 60, No. 3, 2018, pp. 550–591.

[26] Forrester, A. I., Sóbester, A., and Keane, A. J., "Multi-fidelity optimization via surrogate modelling," *Proceedings of the Royal Society A: Mathematical, Physical and Engineering Sciences*, Vol. 463, No. 2088, 2007, pp. 3251–3269.

[27] Sobieczky, H., "Parametric airfoils and wings," *Recent development of aerodynamic design methodologies*, Vieweg+Teubner Verlag, Wiesbaden, Germany, 1999, pp. 71–87.

[28] Kuya, Y., Takeda, K., Zhang, X., and Forrester, A. I., "Multifidelity surrogate modeling of experimental and computational aerodynamic data sets," *AIAA Journal*, Vol. 49, No. 2, 2011, pp. 289–298.

[29] Forrester, A., Sobester, A., and Keane, A., *Engineering design via surrogate modelling: a practical guide*, John Wiley & Sons, Great Britain, Wiltshire, July, 2008.

[30] Lee, T., and Gerontakos, P., "Investigation of flow over an oscillating airfoil," *Journal of Fluid Mechanics*, Vol. 512, 2004, pp. 313–341.

[31] Palacios, F., Alonso, J., Duraisamy, K., Colonno, M., Hicken, J., Aranake, A., Campos, A., Copeland, S., Economon, T., Lonkar, A., et al., "Stanford university unstructured (su 2): an open-source integrated computational environment for multi-physics simulation and design," *51st AIAA Aerospace Sciences Meeting including the New Horizons Forum and Aerospace Exposition*, Grapevine (Dallas/Ft. Worth Region), Texas, January, 2013, p. 287.

[32] Menter, F. R., "Two-equation eddy-viscosity turbulence models for engineering applications," *AIAA Journal*, Vol. 32, No. 8, 1994, pp. 1598–1605.

[33] Abbott, S., *Understanding analysis*, Springer-verlag, New York, 2001.

[34] Chen, G., Xiong, Q., Morris, P. J., Paterson, E. G., Sergeev, A., and Wang, Y., "OpenFOAM for computational fluid dynamics," *Notices of the American Mathematical Society*, Vol. 61, No. 4, 2014, pp. 354–363.

[35] Roy, C. J., "Grid convergence error analysis for mixed-order numerical schemes," *AIAA Journal*, Vol. 41, No. 4, 2003, pp. 595–604.

[36] Kim, Y., and Xie, Z.-T., "Modelling the effect of freestream turbulence on dynamic stall of wind turbine blades," *Computers & Fluids*, Vol. 129, 2016, pp. 53–66.

[37] McKay, M. D., Beckman, R. J., and Conover, W. J., "A comparison of three methods for selecting values of input variables in the analysis of output from a computer code," *Technometrics*, Vol. 42, No. 1, 2000, pp. 55–61.

[38] J. Forrester, A. I., Keane, A. J., and Bressloff, N. W., "Design and analysis of "Noisy" computer experiments," *AIAA Journal*, Vol. 44, No. 10, 2006, pp. 2331–2339.

[39] Thelen, A. S., Leifsson, L. T., and Beran, P. S., "Multifidelity flutter prediction using regression cokriging with adaptive sampling," *Journal of Fluids and Structures*, Vol. 97, 2020, p. 103081.

[40] Raul, V., Leifsson, L., and Koziel, S., "Aerodynamic Shape Optimization for Delaying Dynamic Stall of Airfoils by Regression Kriging," *International Conference on Computational Science*, Springer, Amsterdam, The Netherlands, June, 2020, pp. 57–70.

[41] Kraft, D., et al., "A software package for sequential quadratic programming," Tech. Rep. Report DFVLR-FR 88–28, DLR German Aerospace Center—Institute for Flight Mechanics, Germany, 1988.

[42] Virtanen, P., Gommers, R., Oliphant, T. E., Haberland, M., Reddy, T., Cournapeau, D., Burovski, E., Peterson, P., Weckesser, W., Bright, J., et al., "SciPy 1.0–Fundamental Algorithms for Scientific Computing in Python," *arXiv preprint arXiv:1907.10121*, 2019.